Geophysical Journal International

Geophys. J. Int. (2014) **196,** 633–643
Advance Access publication 2013 October 25

doi: 10.1093/gji/ggt403

An experiment of muon radiography at Mt Etna (Italy)

Daniele Carbone,[1] Dominique Gibert,[2] Jacques Marteau,[3] Michel Diament,[2] Luciano Zuccarello[1] and Emmanuelle Galichet[4]

[1] *Istituto Nazionale di Geofisica e Vulcanologia, Osservatorio Etneo, Sezione di Catania, Catania, Italy. E-mail: carbone@ct.ingv.it*
[2] *Institut de Physique du Globe de Paris (UMR CNRS 7154), Sorbonne Paris Cité, Paris, France*
[3] *Institut de Physique Nucléaire de Lyon (UMR CNRS 5822), Lyon, France*
[4] *Conservatoire National des Arts et Métiers, Paris, France*

Accepted 2013 October 1. Received 2013 October 1; in original form 2013 June 16

SUMMARY

Interactions of conduit geometry with gas–liquid flows control volcanic activity, implying that the evaluation of volcanic hazards requires quantitative understanding of the inner structure of the volcano. The more established geophysical imaging techniques suffer from inherent ambiguity, may require spatially dense measurements in active areas and may not provide sufficient spatial resolution in the uppermost part of the conduit system. It is thus desirable to develop new imaging techniques allowing a better spatial resolution of a volcano's upper feeding system, with reduced ambiguity and a low level of risk for operators.

Muon particles can be utilized to image the internal density distribution of volcanic structures. The principle of muon radiography is essentially the same as X-ray radiography, except for substituting penetrating particles in place of photons. Muons are more attenuated by higher density parts inside the target and thus information about its inner structure are obtained from the differential muon absorption.

We report on a muon-imaging experiment that was conducted at Mt Etna in 2010. The target structure was one of the summit craters of the volcano. This experiment was performed using a muon telescope suitably designed to withstand the harsh conditions in the summit zone of a high volcano.

We found a marked difference between synthetic and observed attenuation of muons through the target. This discrepancy is likely due to the bias on the observed flux, arising from false muon tracks. They are caused by low-energy particles that, by chance, hit simultaneously the two matrixes of the telescope, leading to detection of a false positive. We separated the useful from the unwanted signal through a first-order model of the background noise. The resulting signal is compared with the corresponding synthetic flux. Eventually, we found regions of higher- and lower-than-expected muon flux, that are possibly related to inner features of the target crater.

Key words: Tomography; Volcano monitoring; Volcanic hazards and risks.

1 INTRODUCTION

Volcanic activity involves several phenomena, mainly resulting from complex interactions of conduit geometry with gas–liquid flows. The geometry of the upper plumbing system of an active volcano is, hence, a key feature to model the processes, which may lead to paroxysmal activity. Indeed, parameters such as maximum sustainable conduit overpressure, magma ascent rate, gas volume fraction and volumetric flow rate are all related to conduit shape and size. These observations imply that a detailed knowledge of the shallow underground structure is mandatory to forecast the occurrence of dangerous stages of activity (Gilbert & Lane 2008), and thus to mitigate volcanic hazards.

Moreover, in the presence of complex discharge systems including different eruptive centres, detailed knowledge of conduits and connection structures is useful to understand the coupled process that regulate the activity from the different craters.

To investigate the underground structure of a volcano, different techniques are utilized, that are sensitive to different physical properties of the underground rocks (e.g. elastic and electrical properties and density).

Classic seismic approaches are based on the inversion of earthquake traveltime data, to derive a 3-D image of the velocity structure (Aki *et al*. 1977). Ambient noise interferometry is also increasingly used to image volcanic structures (e.g. Brenguier *et al*. 2007). This method relies on the ambient seismic noise excited by

© The Authors 2013. Published by Oxford University Press on behalf of The Royal Astronomical Society.

GJI Geodynamics and tectonics

Downloaded from https://academic.oup.com/gji/article/196/2/633/571839 by guest on 24 April 2024

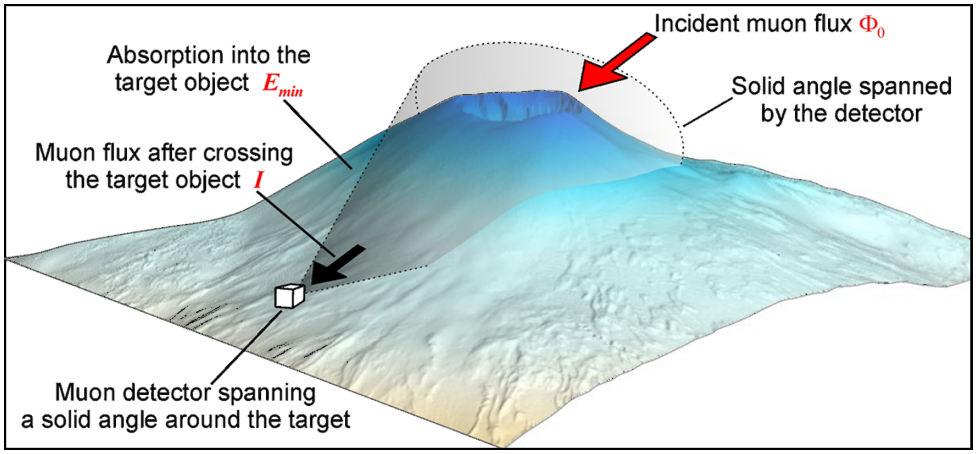

Figure 1. Schematic sketch showing the main issues involved in the muon radiography of volcanoes. The differential incident flux, Φ_0, within the solid angle spanned by the detector, is reduced by absorption inside the target structure. The telescope allows to measure the integrated flux, I, along each incident direction, after the target object is crossed.

shallow sources (ocean microseisms or atmospheric perturbations; Friedrich *et al*. 1998; Tanimoto 1999) and is based on the computation of noise cross-correlations between different receiver pairs, to derive the impulse response of the medium.

The subsurface distribution of electrical properties may be imaged through dc electrical resistivity (e.g. Pessel & Gibert 2003) or low-frequency electromagnetic techniques (e.g. Zhdanov 2009).

Gravity measurements allow the computation of Bouguer anomalies (Deroussi *et al*. 2009), which are reflective of anomalies in the underground density structure (Schiavone & Loddo 2007).

Despite the many exploring techniques, volcano imaging remains challenging, mainly because of the highly heterogeneous character of the structures to be investigated. The latter dictates that dense measurements in active zones (Tiede *et al*. 2005), implying a high level of risk, must be performed to properly describe the relevant features. Strong medium heterogeneities produce marked scattering/attenuation of seismic wave and may result in high resistivity/density contrasts, thus making data inversion highly non-linear. Furthermore, in most cases, the more established geophysical imaging techniques do not offer the spatial resolution needed to properly characterize the shallow part of a volcano's plumbing.

It is thus advisable to explore the possibilities of new imaging techniques allowing a better spatial resolution with reduced ambiguity and a low level of risk for the personnel involved in the field work. As detailed in the following sections, muon imaging has the potential to fulfil these requirements.

2 MUON IMAGING OF VOLCANOES

2.1 Basic principles of muon imaging

Cosmic ray muons are elementary particles, which form in the Earth's atmosphere (typically at an elevation of about 15 km), through interactions between primary cosmic rays, from outer space, and atmospheric molecules (Neddermeyer & Anderson 1937). They constantly bombard the Earth's surface and arrive at angles ranging from vertical to horizontal. Muon particles can travel through large thickness (up to kilometres) of rock, with an energy loss mainly depending on the amount of matter crossed (Nagamine 2003). By measuring the absorption of muons along different paths through a solid body, one can deduce the density distribution in the interior of the target. Thus, cosmic-ray can be used to 'see inside' kilometre-size objects.

The differential flux of incident cosmic muons, Φ_0 (given in $\mathrm{cm^{-2}sr^{-1}s^{-1}GeV^{-1}}$), at the measurement site (Fig. 1), is determined through either Monte Carlo (MC) simulation codes (e.g. Heck *et al*. 1998) that allow to generate a large number of air showers, induced by primary nuclei, and to propagate the computed muon production through the atmosphere, or via analytical modelling of experimental results (e.g. Gaisser 1990; Bugaev *et al*. 1998). Fig. 2 reports Φ_0 for three zenith angles (0°, 60° and 85°), calculated from the analytical model of Bugaev *et al*. (1998), as modified through the empirical parametrization proposed by Reyna (2006). The Bugaev–Reyna model (hereafter referred as the B–R model) allows to calculate the differential muon intensity for all zenith angles and for a wide range of energies. MC (Kudryavtsev 2009) or analytical (Lesparre *et al*. 2010) modelling is also used for determination of the energy absorption along each path length inside the target. In particular, starting from the data reported in Groom *et al*. (2001), it is possible to retrieve, in log–log space, a polynomial model linking thickness of standard rock ($\langle Z/A \rangle = 0.5$; $\rho = 2.65\ \mathrm{g\,cm^{-3}}$) to minimum initial

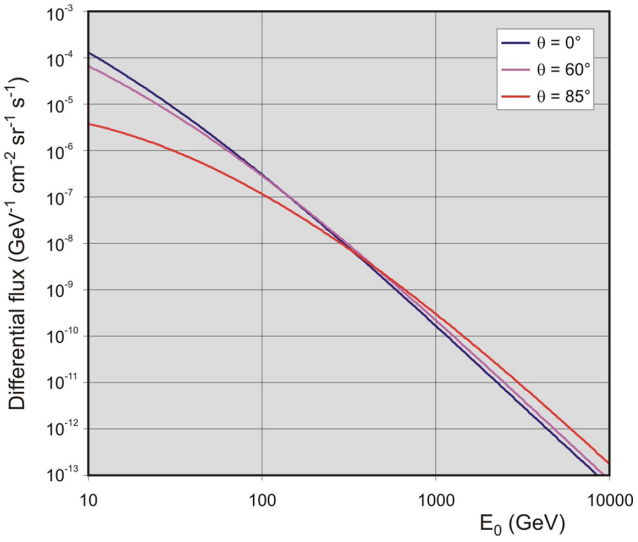

Figure 2. Differential muon flux, calculated through the B–R analytical formulation (see text), for three zenith angles ($\theta = 0°$, 60° and 85°).

Downloaded from https://academic.oup.com/gji/article/196/2/633/571839 by guest on 24 April 2024

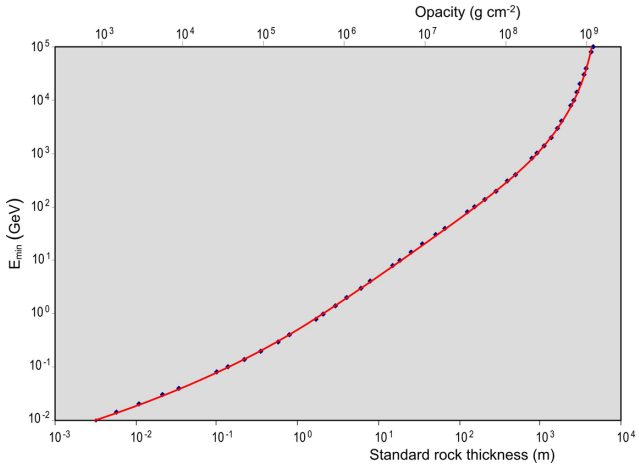

Figure 3. Minimum initial energy ($E_{\min}$) that a muon must have to cross a given thickness of standard rock. Dots are data from Groom *et al*. (2001), while the curve is the best-fitting sixth-order polynomial in log–log space.

energy ($E_{\min}$) necessary for a muon to cross it (Fig. 3). Almost all types of rocks share the same $\langle Z/A \rangle$ ratio and the only varying quantity is the density. Accordingly, the formulation derived for the standard rock can be utilized to calculate $E_{\min}$ relative to other rock types, provided that the product between length of crossed rock and density remains the same. Once $E_{\min}$ is estimated, it can be used to compute the theoretical integrated muon flux, I, after the target object has been crossed (Fig. 1), starting from the model of Φ_0:

$$I = \int_{E_{\min}}^{\infty} \Phi_0 \, \mathrm{d}E_0 \quad [\mathrm{cm}^{-2}\mathrm{sr}^{-1}\mathrm{s}^{-1}]. \tag{1}$$

Muon imaging is accomplished through the comparison between the observed integrated muon flux, after the target object is crossed and the corresponding theoretical flux (eq. 1). The latter is calculated under the assumption of an homogeneous target object using the theoretical incident muon flux, in open sky conditions, and the relevant topographic information. Once the differences between observed and theoretical integrated fluxes are estimated, by knowing the energy loss of muons through matter one can derive anomalies in the amount of matter encountered along each direction by the travelling particles, that is, anomalies in the so-called density length (Tanaka *et al*. 2007) or opacity, ε (Lesparre *et al*. 2010), expressed in g cm^{-2}. Furthermore, if the path lengths insight the target object are known from topographic information, it is possible to retrieve anomalies with respect to the average density of the rock along each travelling direction. Thus, muon imaging furnishes a quasi-direct information about the average density distribution inside the target.

2.2 Application to volcanic structures

Volcano imaging through particle of cosmic origin (muons) is a newly developing technique which has already shown great promise (e.g. Nagamine *et al*. 1995; Nagamine 2003; Tanaka *et al*. 2007, 2009; Lesparre *et al*. 2012; Saracino & Cârloganu 2012). A detector is placed on the flank of a volcano and is used to obtain a 2-D image of the volcano interior projected onto the plane of the detector (Fig. 1). This method presents some advantages with respect to more established geophysical techniques. First of all, it is possible to directly determine the amount of matter crossed along each travel direction of the particles, an information that, by knowing the thickness of crossed rock, can be converted into average density. Thus, the method does not suffer from the inherent ambiguity proper of most geophysical techniques. In fact, thanks to the almost rectilinear trajectories of the muons, the inverse problem becomes relatively simple.

Another advantage of volcano imaging via muons consists in the fact that a natural, fairly constant and widespread source, that is, the muon flux, is utilized, implying that it is not necessary to implement cost demanding energizing systems as when electric or active seismic sources are utilized (e.g. Di Stefano & Chiarabba 2002). Spatially dense measurements in areas not easily accessible are not required as one only needs to deploy the detector(s) in order to perform the muon imaging of the target, also implying a lower risk of injury to personnel operating in the crater area of a volcano. Finally, the spatial resolution can be easily adjusted as a function of the target object through modifying the geometrical characteristics of the muon detector. Under certain circumstances, inner structures inside the target object can be recognized with a spatial resolution as fine as a few tens of meters.

Among the disadvantages of muon imaging, the most important are that: (i) due to geometrical constraints, only the part of the volcanic edifice above the horizon of the detector can be investigated (Fig. 1) and (ii) to have a sufficient flux, the thickness of rock to be crossed by muons should not exceed a few kilometres (Nagamine 2003). Furthermore, the time interval needed to resolve a given density contrast should not exceed the typical period of volcanic processes able to change the internal density distribution of the target structure. Hence, under certain experimental conditions, volcano imaging using muons may prove to be unfeasible.

A preliminary derivation of feasibility conditions for muon imaging of geological objects can be obtained following Lesparre *et al*. (2010), to whom we refer for a complete account. A summary of their findings is reported in the following. Fluctuations in the muon flux are usually assumed to be well described by a Poisson distribution. Assuming that the number, N, of events is large enough and recalling that the variance of a Poisson process equals the number of realizations, to distinguish two nearby opacities (see Section 2.1), that is, $N(\varepsilon_0 + \delta\varepsilon)$ from $N(\varepsilon_0)$, at the 1σ confidence level, the following condition must be satisfied:

$$\Delta N(\varepsilon_0, \delta\varepsilon) > \sqrt{N(\varepsilon_0)}. \tag{2}$$

The above condition may be used to define a first-order relation linking the number of muons recorded during a given amount of time, ΔT, the amount of crossed matter, ε, and the telescope acceptance, Γ (given in cm^2 sr; Gibert *et al*. 2010), the function by which the integrated flux, arriving to the detector planes, can be converted into a number of muons (Lesparre *et al*. 2010):

$$\Delta T \times \Gamma \times \frac{\Delta I^2(\varepsilon_0, \delta\varepsilon)}{I(\varepsilon_0)} > 1. \tag{3}$$

Γ is controlled by the geometrical characteristics of the telescope (Gibert *et al*. 2010) and accounts for its detection area. Despite its limitations due to the inherent assumptions, eq. (3) helps to define the applicability domain of muon imaging. Through this relation it is possible to test the suitability of the method to investigate the density distribution inside a candidate target structure. The left-hand term of the above condition is determined both by the fixed total opacity of the medium ε_0, which depends on the characteristics of the geological target, and by the desired resolution level, $\delta\varepsilon$. This sets the minimum value for the product $\Delta T \times \Gamma$ and the question is to determine whether it is reachable or not (i.e. acquisition time long enough and/or detection area large enough). This will clearly

Downloaded from https://academic.oup.com/gji/article/196/2/633/571839 by guest on 24 April 2024

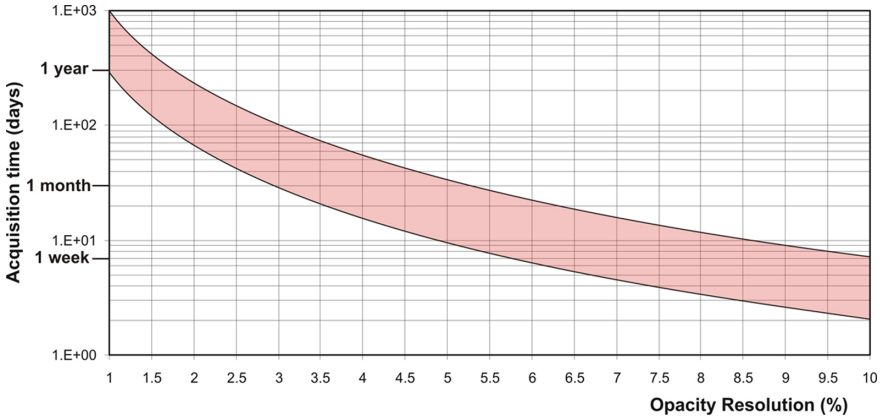

Figure 4. Opacity resolution ($\delta\varepsilon$) that can be achieved after a given acquisition time. In the calculation we assumed (i) telescope acceptance (Γ) $\sim$10 cm^2 sr, target size of 500 m and target density between 1 (lower curve) and 2 g cm^{-3} (upper curve).

depend on the particular constrains attached to a given experimental situation.

Fig. 4 reports the opacity resolution ($\delta\varepsilon$) that can be achieved after a given acquisition time, assuming (i) telescope acceptance $\sim$10 cm^2 sr (a value based on the characteristics of the telescope used at Etna in 2010; see Section 3 and Fig. 7), target size of 500 m and target density between 1 (lower curve) and 2 g cm^{-3} (upper curve). For example, after an acquisition time of 1 month, an opacity resolution of about 3 and 5 per cent (target density of 1 and 2 g cm^{-3}, respectively) can be reached. This results implies that, if the inner structure has a density equal to one-half that of the surrounding, it must have a size of about 30 and 50 m to be detected, in the cases of lower and higher target density, respectively.

2.3 The interest of applying muon imaging to study Mt Etna

Mt Etna, one of the most active and well-studied volcanoes in the world, is a large (1200 km^2) strato-volcano with a base diameter of about 40 km and a height of about 3350 m. It is sited on the East coast of Sicily (Italy), near a densely populated area (Fig. 5). Mt Etna is persistently active, with almost permanent degassing occurring from the summit craters. Etna's eruptions occur either at its four summit craters (Voragine, Bocca Nuova, Northeast Crater and Southeast Crater; see Fig. 5) or from vents or fissures on its flanks. During the last decade, Mt Etna has been characterized by eruptions exhibiting a wide range of explosive behaviour (Behncke & Neri 2003), including episodes of vigorous fire-fountaining, often accompanied by emission of ash columns up to some kilometres above the summit craters (Allard *et al*. 2005; Andronico *et al*. 2008). The associated widespread tephra falls have had a severe impact on the economy of Eastern Sicily, mainly due to the troubles it caused to air traffic, road traffic and crops. Therefore, even thought Etna's activity is not considered to represent an acute hazard to human lives, it is important to comprehensively understand the magma dynamics at this volcano and quantify the factors that may tip it out of its dynamic equilibrium into paroxysm. Quantitative information on the subsurface structure of Mt Etna represents a key constraint on the possibility of gaining further insights into its shallow dynamics.

The shallow conduit network feeding the four summit craters of Etna is best envisioned as a plexus of dikes and sills (De Gori *et al*. 2005), whose geometry is still largely unknown. Muon imaging could help to improve our knowledge of this complex system, thus allowing to better understand processes that can trigger paroxysmal events (i.e. rising of gas slugs, accumulation of foam layers, etc.). The interpretation of many different signals would benefit from this unprecedented information. For example, determination of seismic source parameters from moment tensor inversion (Lokmer *et al*. 2007; De Barros *et al*. 2011), localization of the volcanic tremor source (Di Lieto *et al*. 2007), localization and quantification of the underground mass redistributions responsible for gravity anomalies observed at the surface (Carbone *et al*. 2008) would be more reliable and accurate if a clearer image was available of how the different subsystems feeding the summit craters are shaped, work and are interconnected to each-other. Furthermore, some specific "open questions" could be addressed about the structural control exerted on (i) the shallow (about 500 m below the surface) source volume where the non-destructive process inducing propagation of VLP seismic waves takes place (Saccorotti *et al*. 2007);

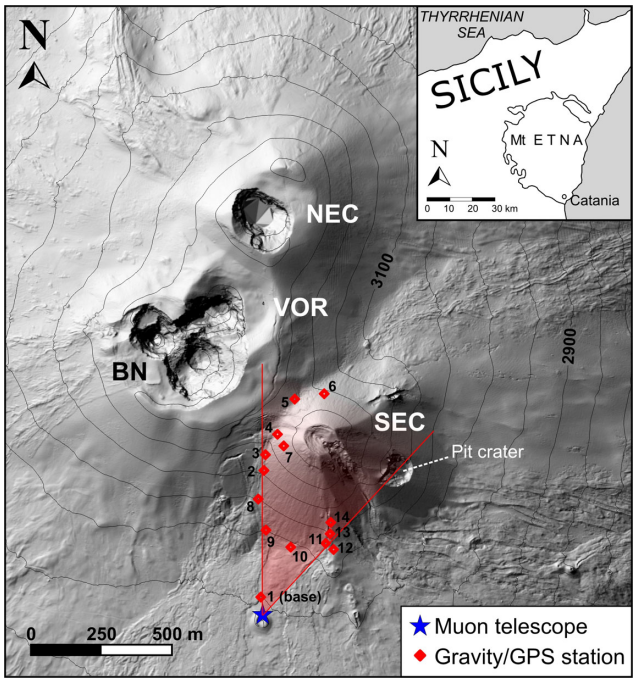

Figure 5. Map showing the four craters in the summit zone of Mt Etna (NEC, Northeastern Crater; VOR, Voragine; BN, Bocca Nuova; SEC, Southeastern Crater). The blue star shows the position of the muon telescope, whose azimuthal viewing angle is marked through red lines. The red diamonds show the position of the gravity/GPS benchmarks.

Downloaded from https://academic.oup.com/gji/article/196/2/633/571839 by guest on 24 April 2024

(ii) the horizontal migrations of the volcanic tremor source at shallow depths, during particular phases of the volcanic activity (e.g. Di Grazia *et al*. 2006; Aiuppa *et al*. 2010) and (iii) the mechanisms controlling eruption inception, progression and shift between eruptive styles (e.g. Carbone *et al*. 2006).

3 THE 2010 MUON EXPERIMENT AT MT ETNA

The first experiment of muon radiography at Mt Etna was performed in the summer of 2010. The aim of this experiment was twofold: (1) test the performance of our (at the time) newly designed telescope for outdoor applications under the very severe conditions encountered in the summit zone of Etna and (2) check whether it was actually possible to assess the high data-quality claimed by previous studies (Tanaka *et al*. 2009), under similar experimental conditions.

The Southeastern Crater (SEC), one of the four active craters in the summit area of the volcano (Fig. 5), was chosen as a target. Under the conditions of the experiment, this crater was found to be the more appropriate target due to both its size and position. Even though the imaging of a larger portion of the edifice, comprising the uppermost part of the system feeding the craters, would have been more interesting from the scientific standpoint, more acquisition time and detection area (i.e. a larger-sized detector) would have been needed (see eq. 3). In the framework of a temporary deployment, the choice of the SEC as a target was made as a compromise between technical feasibility and time restraints.

The SEC is about 240 m tall (from 3050 to 3290 m a.s.l.), with a base diameter of about 500 m. The muon detector was installed on its southern slope, ∼650 m away from the summit. This point allows to image the target with minimal shadow effect from the other summit craters (Fig. 5).

The muon detector (telescope) that was utilized at Mt Etna in the framework of the 2010 experiment (Fig. 6a) is identical to the one described by Lesparre *et al*. (2010) and by Marteau *et al*. (2012) and we refer to those papers for a detailed description. In the following we only provide a summary of the main detector characteristics. The telescope employs plastic scintillator strips, arranged in two orthogonal series of X rows and Y columns, to form a matrix plane. When a muon hits a detector matrix, the X and Y bars, whose intersection forms the crossed pixel (Fig. 6b), emit UV light. The latter is captured by active fibres (WLS), running longitudinally along the axis of each scintillator bar, transformed in visible green light, and transmitted, through optical fibres, to a photomultiplier, each of whose channels corresponds to one pixel in the matrix. If two (or more) parallel planes are utilized, by knowing which pixels in the front and the rear matrixes of the telescopes are hit, one can determine the arriving trajectory of the particle (Fig. 6b). The telescope readout system is adapted from that developed under the OPERA experiment (Marteau 2010). It consists of a multi-anode photomultiplier tube (MaPMT) connected to an acquisition board (Ethernet Controller Module), which allows to recognize quasi-simultaneous events (i.e. within 10 ns; Lesparre *et al*. 2012) in the two matrixes. Such events are considered as due to a single muon particle hitting the two planes and are recorded in the database for further post-processing.

The muon telescope installed on Etna in 2010 consisted of two detection planes, both with 16 X and 16 Y strips, to form 256 pixels, each sized 5 × 5 cm^2. The planes were mounted on a specifically designed aluminum frame (Fig. 6a) with adjustable legs (to cope with the uneven terrain), allowing to precisely set in the field both the interplanes distance and the orientation of the planes towards the geological target (Lesparre *et al*. 2010). The interplanes distance was set to 170 cm, which implies a space resolution of less than 20 m, taking into account the telescope-target distance (∼650 m; Fig. 5). The telescope zenith angle was set to 73°. Fig. 7 reports the acceptance (Section 2.2) corresponding to the above telescope configuration. The shape of the acceptance function accounts for the fact that a different detection area corresponds to the different arriving directions in the solid angle spanned by the detector (see Gibert *et al*. 2010 for a detailed discussion of this topic).

In order to improve the signal-to-noise ratio, Nagamine *et al*. (1995) suggested the use of a threefold telescope. Nevertheless, Tanaka *et al*. (2009) claimed that good imaging performance can be achieved using a twofold detector. The data discussed by Tanaka *et al*. (2009) were collected in conditions very similar to the ones we encountered at Etna, in terms of (i) target size, (ii) detector-target distance and (iii) detector characteristics. Based on these premises, to image Etna's SEC, we decided to employ a detector featuring only two detection planes. It is worth stressing that, in the summit zone of a high volcano, where, due to the lack of roads, there may be the need to cover on feet some distance to the installation sites, the choice of a detector consisting of either two or more than two detection planes may be critical (each ∼1 × 1 m^2 plane of the detector we utilized has a weight of about 80 kg).

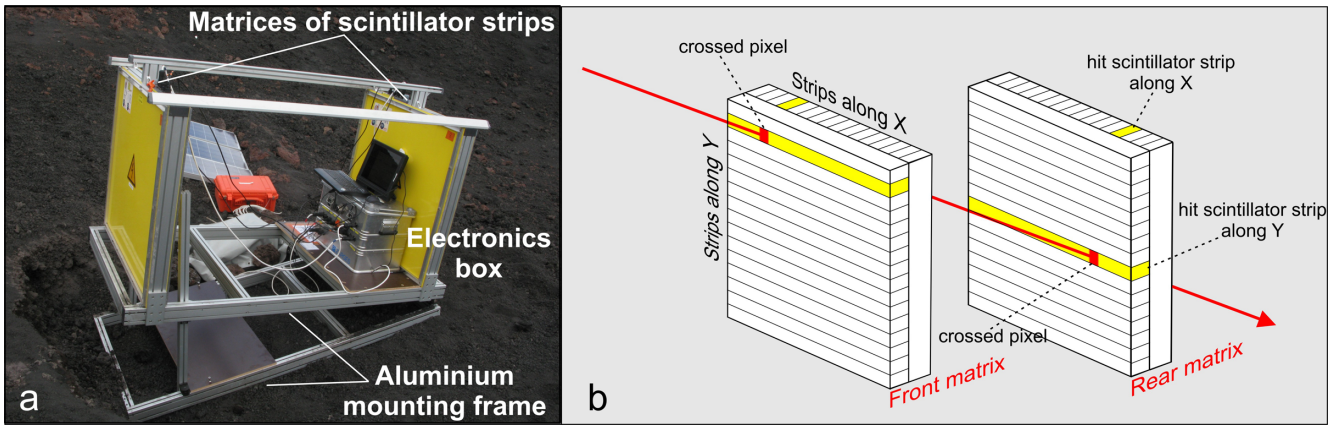

Figure 6. (a) The muon telescope in operation at Etna during the summer of 2010. The two detection planes, the metal box containing the electronics and the aluminium mounting frame are visible. (b) Functioning scheme of a muon telescope featuring scintillator bars: a muon hits two pairs of X and Y strips in the front and rear matrixes, respectively, allowing the incident direction (red arrow) to be retrieved.

Downloaded from https://academic.oup.com/gji/article/196/2/633/571839 by guest on 24 April 2024

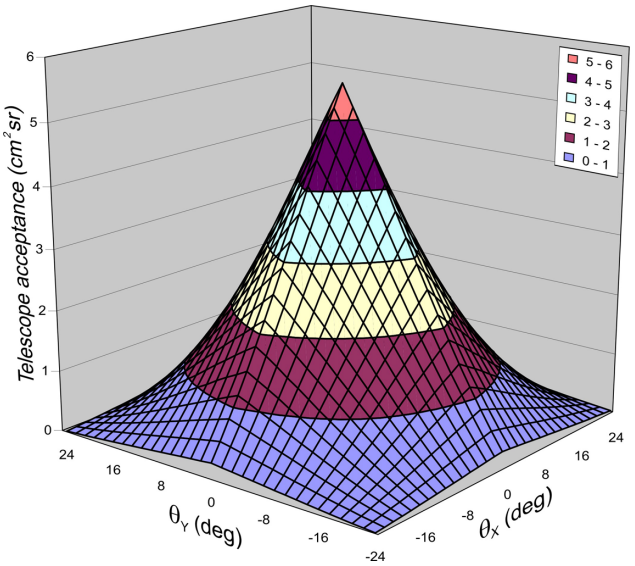

Figure 7. 3-D representation of the acceptance function (Γ), for each discrete direction of sight of the matrix pair. This acceptance corresponds to the configuration of the telescope installed at Etna in 2010 (two 16 × 16 matrices, with pixel size of 5 cm and separated by 170 cm).

During the summer of 2010 gravity and precise positioning (GPS) measurements were also performed on the SEC area, aimed at complementing the results from muon imaging.

4 DATA PRESENTATION

In the framework of the Etna experiment, the rock thickness crossed by each muon track in the solid angle spanned by the telescope was calculated using the high-resolution DEM developed by Favalli *et al*. (2009) from LiDAR data (Fig. 5). This model furnishes a very accurate representation of the SEC at the time of the muon experiment. Apart from the high thicknesses in the westernmost part of the image, due to shadow effects from the other craters (i.e. Voragine and NE Crater; see Fig. 5), the muon tracks arriving to the telescope cross up to ∼800 m of rock (Fig. 8).

An acquisition time of around 150 days was scheduled for the 2010 Etna experiment. However, technical issues, related to the harsh conditions in the installation site, limited the acquisition time

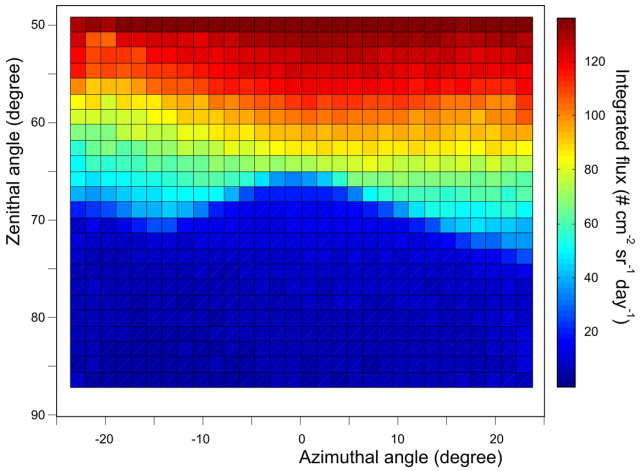

Figure 9. Observed integrated muon flux, after an acquisition time of about 30 days.

to about one month (during the 2010 August–October interval). It is worth stressing that the results presented by Tanaka *et al*. (2009) were also obtained after an acquisition time of about 1 month. The integrated muon flux (in $\#cm^{-2}sr^{-1}s^{-1}$) measured during 2010 Etna experiment is presented in Fig. 9. The topographic profile from the point of view of the telescope (right-hand panel of Fig. 8) is well reproduced in the muon image (Fig. 9), due to the abrupt flux change when passing from *open-sky* (*os*) to *through-crater* (*tc*) conditions.

The validity of the data acquired during the 2010 experiment can be tested via comparison with a theoretical model. In particular, we compared the observed and calculated attenuation of the muon flux, due to the absorption of the particles into the target. The observed muon attenuation is given, for each incident direction, by the ratio between the integrated flux after the crater is crossed and the corresponding flux in *os* conditions. During the 2010 Etna experiment a measurement of the integrated muon flux in *os* conditions was performed at the installation site, before turning the telescope towards the target object. The observed muon attenuation along the azimuthal direction perpendicular to the planes of the telescope is shown in Fig. 10(a) (red curve), plotted against the zenithal angle.

The definition of the theoretical attenuation requires a model describing the differential incident flux (Φ_0) and the computation of the energy loss of muon particles travelling inside rock. We

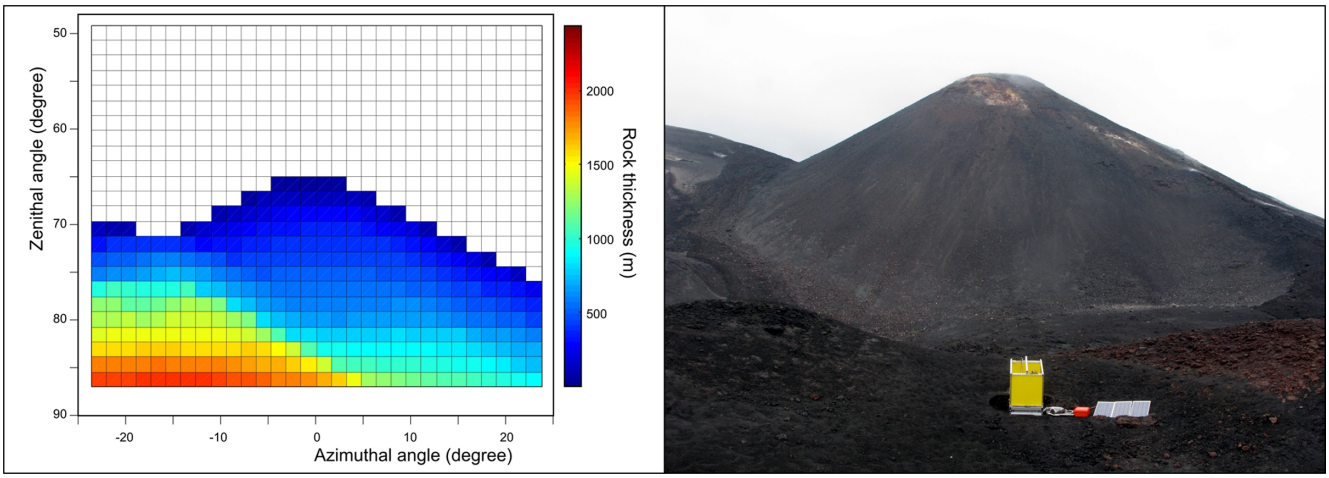

Figure 8. Left-hand panel: rock thicknesses along the directions in the solid angle spanned by the telescope. The white area on the top of the image indicates open sky. Right-hand panel: the SEC viewed from behind the telescope.

Downloaded from https://academic.oup.com/gji/article/196/2/633/571839 by guest on 24 April 2024

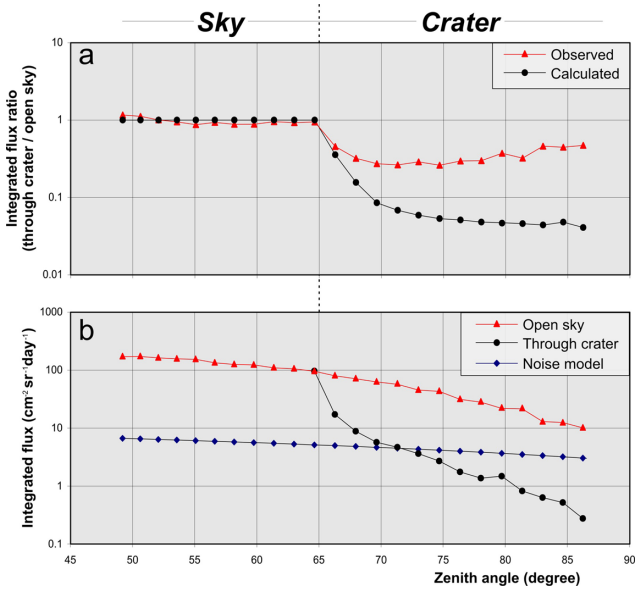

Figure 10. (a) Observed (red curve) and calculated (black curve) *tc*/*os* flux ratios along the middle azimuthal direction of the telescope. The synthetic ratio is calculated assuming an average bulk density of the SEC of 0.7 g cm^{-3}. (b) Observed *tc* (black curve) and *os* (red curve) integrated fluxes along the middle azimuthal direction of the telescope. Both *tc* and *os* curves are corrected for the estimated background noise (blue curve).

obtained a representation of Φ_0 through the B–R analytical model (Section 2.1; Fig. 2). To compute the energy loss of muons in the target, we utilized the polynomial model that relates $E_{\min}$ to opacity of rock in log–log space (Section 2.1; Fig. 3). The determination of the relevant opacities requires the knowledge of (i) the thickness of rock crossed along each arriving direction and (ii) the average bulk density of the target. The first information can be retrieved from the available topographic data (Favalli *et al*. 2009; Fig. 8). The gravity/GPS data collected during the summer of 2010 can be utilized to set constraints on the average bulk density of the target structure.

5 BULK DENSITY OF THE TARGET FROM GRAVITY/PRECISE POSITIONING MEASUREMENTS

Among the methods that can be exploited to complement the information from muon imaging, gravimetry is one of the most suitable since it is also directly related to the underground density structure. When used for subsurface imaging, gravity measurements need to be reduced for the difference in altitude between the reference and the observation points (free-air correction) and for the effect of the different distribution of above-ground masses around each measurement point (terrain correction). Once these corrections are accomplished, gravity measurements are reduced to Bouguer anomalies (Deroussi *et al*. 2009), which reflect anomalies in the subsurface density structure. The accuracy of Bouguer anomalies depends on the quality of field measurements and on the accuracy of free-air and terrain corrections. In turn, the latter depends on how precise are (i) the vertical positioning of the gravity sensor and (ii) the elevation model of the area of interest.

During the summer of 2010 gravity/GPS measurements were accomplished at 14 benchmarks, including a reference base, at elevations ranging between 3000 and 3224 m a.s.l. (Fig. 5). A relative

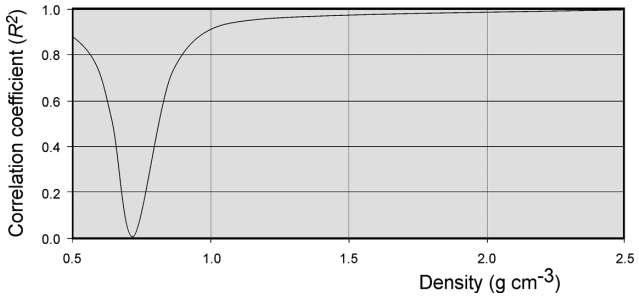

Figure 11. Correlations between residual Bouguer anomalies and elevation, plotted against average bulk density.

spring gravimeter (CG-5 by Scintrex) and a Trimble handheld GPS receiver were utilized. We adopted a suitably designed strategy of gravity measurement that allowed to accurately estimate the effect of instrumental drift and to recognize *tares* (Rymer 1989). The average measurement error was equal to 10 microGal. We improved the accuracy of GPS positioning in post-processing, towards a few mm, by exploiting the reference signal from the four continuous GPS stations operating on Etna, at elevations above 2600 m (Bruno *et al*. 2012). Finally, to perform the terrain correction, we used the accurate DEM by Favalli *et al*. (2009).

The Bouguer values obtained after applying the above corrections were used to determine the average bulk density of rocks in the area of interest, through the density-dependent gravity-height relationship. Indeed, following Nettleton (1939), Bouguer anomalies, if computed with corrected density values, behave as stochastic quantities which are not correlated with point elevation and, thus, the best average density is sought as the one allowing minimal correlation (Schiavone & Loddo 2007). From this analysis, it results an average bulk density of 0.7 g cm^{-3} (Fig. 11). This surprisingly low value may depend on (i) the low density of the highly vesiculated rocks that make most of the SEC and (ii) the presence of cavities inside the crater due to both syn- (low packing density) and post-depositional processes. With reference to the second above point, it is important to stress that the density value we found represent the average bulk density of the whole structure (SEC), rather than the density of the rocks that form it.

6 DISCUSSION

Even assuming the low average bulk density of the target structure which results from the analysis of the gravity/precise positioning measurements (0.7 g cm^{-3}; see previous section and Fig. 11), the expected attenuation of the muon flux due to the SEC exceeds the corresponding observed attenuation by a factor of up to about 10 (Fig. 10a). This discrepancy is likely due to severe background noise from false muon tracks (Nagamine *et al*. 1995). The latter may arise from low-energy particles (mostly electrons, but also positrons) that, by chance, hit simultaneously the two matrixes of the telescope (Nagamine 2003), leading to detection of a false positive. If the fictitious flux induced by the false events exceeds the weak flux of muons emerging from the crater, important distortions may occur in the integrated *tc* /*os* flux ratio, like the one we observed (Fig. 10a).

The integral vertical intensity of electrons at the sea level is very approximately 35 m^{-2}s^{-1}sr^{-1} (Allkofer & Grieder 1984). The exact number is difficult to determine because of the different altitude dependence of the different sources of electrons (Daniel & Stephens 1974). Results of extended MC simulations of air shower (Tanaka & Muraoka 2013) indicate that the ratio, *r*, between (i) integral

Downloaded from https://academic.oup.com/gji/article/196/2/633/571839 by guest on 24 April 2024

intensity of muons at zenith angles $>50^\circ$ and $>70^\circ$ (horizontal muons) and (ii) integral vertical intensity of EM particles with multiplicity ≥ 2 (at last two simultaneous hits) ranges between 100:8 and 1:1 (Tanaka, personal communication, 2012). Taking into account the inclination of the telescope installed at Etna in 2010 (73°; see Section 3), which controls the vertical and horizontal projected areas of the detection planes, through the above range we found that a value of r between about 3 and 40 is expected under the conditions of the 2010 Etna experiment.

We derived, through linear regression analysis, a first-order approximation of the integrated fictitious flux (Fig. 10b). In practice, we calculated the difference between observed and synthetic flux along the middle azimuthal direction of the telescope and, under the assumption that the discrepancy between observed and synthetic data is mainly due to the false muon tracks, we used the best-fitting linear regression of this difference versus zenith angle as a model for the background noise (blue curve in Fig. 10b). The variability of the difference between observed and synthetic flux is very well explained by the linear regression on the independent variable, as indicated by the high value of the coefficient of determination ($R^2 = 0.90$). The standard deviation of the linear regression model is equal to 0.35 $m^{-2}s^{-1}sr^{-1}$. The background noise model was calculated only along the middle azimuthal direction of the telescope, to which the largest detection area corresponds (Section 3; Gibert *et al*. 2010). Accordingly, this direction offers the most favourable signal-to-noise ratio, thus allowing to achieve the most accurate result.

The expected range of values for r at the installation site, derived from MC calculations, roughly agrees with the corresponding one arising from our first-order noise model. Indeed, the ratio between (i) the observed flux in *os* conditions ($50^\circ <$ zenith angle $< 80^\circ$) and (ii) the model of the integrated fictitious flux ranges between about 5 and 30 (Fig. 10b). It is important to note that the fictitious flux model exceeds the weak *tc* flux by a factor of up to 10, at zenith angles between 70° and 85°. Lesparre *et al*. (2010) estimated that, under various experimental conditions, the small anomalies in the integrated *tc* flux, possibly related to density inhomogeneities inside geological target structures, amount to a small fraction of the total signal. Detection of such small anomalies thus requires a very accurate evaluation of the background noise, which should take into account all the relevant pieces of information.

From the above observations, it appears that, due to the strong background noise from false muon tracks, it not feasible to use the data acquired at Etna to obtain precise quantitative information on the density distribution inside the SEC. However, qualitative understanding can be gained through the first-order noise model we derived. In particular, we performed a comparison between the synthetic and observed *tc* fluxes (Fig. 12). The former was calculated under the assumption of a homogeneous target, while the latter was obtained after correcting the data for the estimated noise. The "coherent" regions of higher- and lower-than-expected muon flux that appear in Fig. 12 may be roughly representative of the density inhomogeneities encountered by the muon particles while travelling through the target.

Overall, we found a fair agreement between synthetic and observed *tc* fluxes (flux differences close to zero), implying either (i) that the size of most anomalous volumes inside the target is smaller than the space resolution of the detection system (Section 3), or (ii) that most of the opacity anomalies are below the resolution threshold imposed by the constraints discussed above (i.e., ΔT, Γ and ε_0 in eq. 3), or (iii) that remarkable density anomalies inside the target are mostly missing.

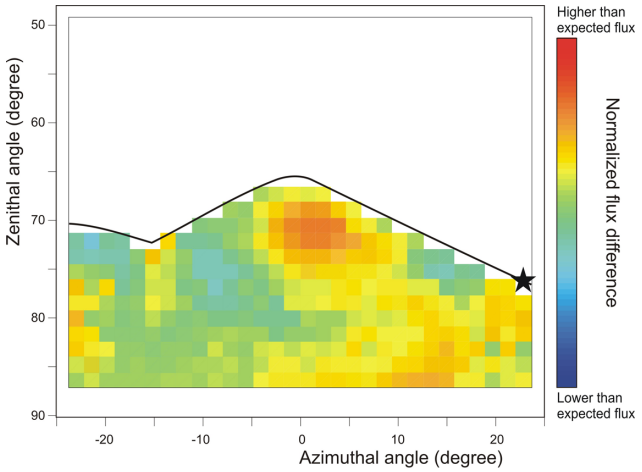

Figure 12. Normalized residual flux after subtracting a synthetic model (calculated under the assumption of an homogeneous target) from the *tc* observed flux (corrected for background noise; see text for details). The black star represents the projected position of the pit crater on the east flank of the SEC (Fig. 5).

The most striking feature appearing in Fig. 12 is the excess of flux in the central part of the image, which involves muon tracks passing through the upper part of the crater. This result could indicate that a lower opacity than expected is encountered along the above tracks, an interpretation which is reasonable if one considers that more altered material (highly fumarolized rocks) is likely to form the volume at the top of the central conduit throughout the cone. Furthermore, the right-hand side of the residual flux image is characterized by a tendency towards excessive flux (Fig. 12). A fissure system cuts the SE flank of the SEC (Behncke *et al*. 2006) and represent the surface expression of a weakness zone across that sector of the cone, a feature that could explain the higher-than-expected flux values. During the past years this structure channelled the flow of magma from the shallowest portions of the central conduit to vents on the eastern slope of the SEC, like in the cases of the 2006 July (Ferlito *et al*. 2010), 2006 November (Sciotto *et al*. 2011) and 2007 August–September (Andronico *et al*. 2008) eruptive episodes. Some collapses also occurred along this fissure system, leading to the formation of pit carters and testifying the presence of underground void spaces. The pit crater that formed in 2007 (Figs 5 and 13) has become ever since the most active structure of the SEC (its projected position is reported in Fig. 12 with a black star). Indeed, lava fountains episodes occurred from this crater in 2007 September, 2007 November and 2008 May (Aiuppa *et al*. 2010). Throughout 2011, 18 lava fountains rose from the same vent, eventually leading to the formation of a large pyroclastic cone around the former pit crater (Patanè *et al*. 2013). Neri & Acocella (2006) proposed that the large-scale dynamics of Etna edifice may alter the stress field and deformation pattern on the volcano's summit, leading to the formation of local fracture systems that play an important role in the movements of magma at shallow levels. The southeastern migration of the main vent of the SEC from the top of the original cone to its east flank has been probably controlled by one of the above local structural features, whose shallowest portion is supposed to have caused the higher-than-expected values in right-hand side of the residual flux image (Fig. 12).

Our results encourage the implementation of further muon imaging experiments which have the potential to provide important details on the structures controlling the activity from the summit craters of Etna. Indeed, also considering our results on the low bulk

Downloaded from https://academic.oup.com/gji/article/196/2/633/571839 by guest on 24 April 2024

Figure 13. Ash emission from the pit crater on the east flank of the SEC in 2008 May.

density of the SEC (Section 5), by using a telescope featuring a larger detection area, it would be possible to investigate a wider portion of the volcanic edifice of Etna than possible in the framework of the 2010 experiment (see Section 2.2). Unprecedented information could be gained on the shallow structures that are thought to connect the plumbing systems of the different summit craters. The existence of such structural links has only been hypothesized on the grounds of geological (Neri & Acocella 2006), geophysical (Sciotto *et al*. 2011) and geochemical (Aiuppa *et al*. 2010) observations. Muon imaging could provide new insight into the shape, position and size of these features, thus deriving unprecedented constrains on models aimed at describing and forecasting the summit eruptive activity of Etna.

7 CONCLUSIVE REMARKS

As shown in past studies, (Nagamine 2003; Tanaka *et al*. 2009; Lesparre *et al*. 2012), muon imaging is a promising tool to investigate volcanic structures. It allows to quasi-directly probe the internal density distribution inside volcanoes, with a space resolution (as fine as a few tens of meters, under certain conditions) that could not be attained with other imaging techniques. The drawback is that only targets with limited size and above the horizon of the detector can be investigated. Despite these limitations, muon imaging offers unique possibilities, especially if it is utilized in conjunction with other methods (e.g. Lesparre *et al*. 2012).

In the summer of 2010 we performed a muon experiment at Mt Etna. The SEC, one of the four summit craters of the volcano (Fig. 5), was chosen as a target. This experiment allowed to derive important technical know-how that can be utilized to inform future similar applications. The detection system that we developed to perform muon radiographies of active volcanoes (Fig. 6; Marteau *et al*. 2012), based on plastic scintillator bars, proved to be rugged enough to withstand the harsh conditions in the summit zone of a high volcano like Etna, even in the absence of an hosting building. Issues like strong diurnal temperature changes (we measured values up to 15 °C), strong wind, presence of corrosive gases, erosive ash and, since the second half of September, snow and ice did not prevent the system from working properly. In the framework of the experiment we could also improve our understanding of specific technical issues associated with muon flux measurements in hostile outdoor conditions.

The detection power (in terms of space and density resolution) which is achievable under a given set of experimental conditions mainly depends on target size, acquisition time and detector characteristics. Eq. (3) allows for the determination of the opacity resolution that can be reached after a given acquisition time and using a muon telescope that features a given detection surface (Fig. 4). However, as also demonstrated by our results, the actual detection performance depends on how noise from false muon tracks interferes with the real muon flux. In a recent paper, Shinohara & Tanaka (2012) reviewed the results of Tanaka *et al*. (2009), who performed a muon radiography of Satsuma-Iwojima volcano (Japan), under experimental conditions very similar to those we encountered at Mt Etna. Shinohara & Tanaka (2012) concluded that an important background noise level, arising from fake muon tracks, affects the signal discussed by Tanaka *et al*. (2009), inducing a significant bias that increases towards the bottom part (muon directions at larger zenith angles) of the density radiography they obtained.

The effect of false muon tracks can be drastically reduced through the use of more than two detection planes. Indeed, it can be proven that the probability of fortuitous events is much lower if three or more simultaneous coincidences must occur, rather than only two (Nagamine *et al*. 1995; Lesparre *et al*. 2012). This probability can be further reduced to acceptable levels by imposing the condition that the pixels hit in the different matrixes must be aligned along a straight line (Lesparre *et al*. 2012). These observations imply that, despite the logistic difficulties of transporting heavier equipment in hostile environments, the use of a telescope featuring three or more planes is mandatory when small differences in the integrated muon flux, like the ones induced by density inhomogeneities inside a volcano, must be precisely measured.

We performed a first order correction of the observed *tc* flux, aimed at separating the useful signal from the background noise arising from false muon tracks. With respect to a synthetic flux obtained through analytical modelling, the corrected *tc* flux shows a positive anomaly that could reflect an opacity lower than expected in correspondence of the upper part of the SEC's central conduit (Fig. 12). Within its inherent strong limitations, this results suggests that highly fumarolized rocks form the bulk of this volume. Moreover, values are generally higher-than-expected in the right-hand part of the residual flux image (Fig. 12), possibly due to the presence of a well-known weakness zone across the southeastern sector of the SEC cone.

ACKNOWLEDGEMENTS

We are grateful to N. Lesparre, G. Politi, S. Rapisarda, Jean de Bremond d'Ars and Serge Gardien who took part in the installation and maintenance of the muon telescope. A. Peyrefitte and H. LeMevel contributed to the collection and analysis of the gravity data. Thanks are due to A. Bonforte who processed the GPS data. We acknowledge the financial support from the UnivEarthS Labex program of Sorbonne Paris Cité (ANR-10-LABX-0023 and ANR-11-IDEX-0005-02).

REFERENCES

Aiuppa, A. *et al.*, 2010. Patterns in the recent 2007–2008 activity of Mount Etna volcano investigated by integrated geophysical and geochemical observations, *Geochem. Geophys. Geosyst.,* **11,** Q09008, doi:10.1029/2010GC003168.

Aki, K., Christoffersson, A. & Husebye, E.S., 1977. Determination of three-dimensional seismic structure of the lithosphere, *J. geophys. Res.,* **82,** 277–296.

Downloaded from https://academic.oup.com/gji/article/196/2/633/571839 by guest on 24 April 2024

Allard, P., Burton, M. & Murè, F., 2005. Spectroscopic evidence for a lava fountain driven by previously accumulated magmatic gas, *Nature,* **433,** 407–410.

Allkofer, O.C. & Grieder, P.K.F., 1984. *Cosmic Rays on Earth, Nr 25-1,* Fachinformationszentrum Energie, Physik, Mathematik, Karsruhe, 379 pp.

Andronico, D., Cristaldi, A. & Scollo, S., 2008. The 4–5 September 2007 lava fountain at South-East Crater of Mt Etna, Italy, *J. Volc. Geotherm. Res.,* **173,** 325–328.

Behncke, B. & Neri, M., 2003. The July–August 2001 eruption of Mt. Etna (Sicily), *Bull. Volcanol.,* **65,** 461–476.

Behncke, B., Neri, M., Pecora, E. & Zanon, V., 2006. The exceptional activity and growth of the Southeast Crater, Mount Etna (Italy), between 1996 and 2001, *Bull. Volcanol.,* **69,** 149–173.

Brenguier, F., Shapiro, N.M., Campillo, M., Nercessian, A. & Ferrazzini, V., 2007. 3-D surface wave tomography of the Piton de la Fournaise volcano using seismic noise correlations, *Geophys. Res. Lett.,* **34,** L02305, doi:10.1029/2006GL028586.

Bruno, V., Mattia, M., Aloisi, M., Palano, M., Cannavò, F. & Holt, W.E., 2012. Ground deformations and volcanic processes as imaged by CGPS data at Mt. Etna (Italy) between 2003 and 2008, *J. geophys. Res.,* **117,** B07208, doi:10.1029/2011JB009114.

Bugaev, E.V., Misaki, A., Naumov, V.A., Sinegovskaya, T.S., Sinegovsky, S.I. & Takahashi, N., 1998. Atmospheric muon flux at sea level, underground, and underwater, *Phys. Rev. D.,* **58,** 054001, doi:10.1103/PhysRevD.58.054001.

Carbone, D., Zuccarello, L., Saccorotti, G. & Greco, F., 2006. Analysis of simultaneous gravity and tremor anomalies observed during the 2002–2003 Etna eruption, *Earth planet. Sci. Lett.,* **245,** 616–629.

Carbone, D., Zuccarello, L. & Saccorotti, G., 2008. Geophysical indications of magma uprising at Mt Etna during the December 2005 to January 2006 non-eruptive period, *Geophys. Res. Lett.,* **35,** L06305, doi:10.1029/2008GL033212.

Daniel, R.R. & Stephens, S.A., 1974. Cosmic-ray-produced electrons and gamma rays in the atmosphere, *Revs. Geophys. Space Sci.,* **12,** 233–258.

De Barros, L., Lokmer, I., Bean, C.J., O'Brien, G.S., Saccorotti, G., Métaxian, J.-P., Zuccarello, L. & Patanè, D., 2011. Source Mechanism of Long Period events recorded by a high density seismic network during the 2008 eruption on Mt Etna, *J. geophys. Res.,* **116,** B01304, doi:10.1029/2010JB007629.

De Gori, P., Chiarabba, C. & Patanè, D., 2005. Qp structure of Mount Etna: constraints for the physics of the plumbing system, *J. geophys. Res.,* **110,** B05303, doi:10.1029/2003JB002875.

Deroussi, S., Diament, M., Feret, J. B., Nebut, T. & Staudacher, T.H., 2009. Localization of cavities in a thick lava flow by microgravimetry, *J. Volc. Geotherm. Res.,* **184,** 193–198.

Di Grazia, G., Falsaperla, S. & Langer, H., 2006. Volcanic tremor location during the 2004 Mount Etna lava effusion, *Geophys. Res. Lett.,* **33,** L04304, doi:10.1029/2005GL025177.

Di Lieto, B., Saccorotti, G., Zuccarello, L., La Rocca, M. & Scarpa, R., 2007. Continuous tracking of volcanic tremor at Mount Etna, Italy, *Geophys. J. Int.,* **169**(2), 699–705.

Di Stefano, R. & Chiarabba, C., 2002. Active source tomography at Mt. Vesuvius: constraints for the magmatic system, *J. geophys. Res.,* **107**(B11), 2278, doi:10.1029/2001JB000792.

Favalli, M., Fornaciai, A. & Pareschi, M.T., 2009. LiDAR strip adjustment: application to volcanic areas, *Geomorphology,* **111,** 123–135.

Ferlito, C., Viccaro, M., Nicotra, E. & Cristofolini, R., 2010. Relationship between the flank sliding of the South East Crater (Mt. Etna, Italy) and the paroxysmal event of November 16, 2006, *Bull. Volcanol.,* **72,** 1179–1190.

Friedrich, A., Krüger, F. & Klinge, K, 1998. Ocean-generated microseismic noise located with the Gräfenberg array, *J. Seismol.,* **2**(1), 47–64.

Gaisser, T., 1990. *Cosmic Rays and Particle Physics,* 296 pp., Cambridge University Press.

Gibert, D., Beauducel, F., D´eclais, Y., Lesparre, N., Marteau, J., Nicollin, F. & Tarantola, A., 2010. Muon tomography: plans for observations in the Lesser Antilles, *Earth Planets Space,* **62,** 153–165.

Gilbert, J.S. & Lane, S.J., 2008. The consequences of fluid motion in volcanic conduits, in *Fluid Motions in Volcanic Conduits: A Source of Seismic and Acoustic Signals,* pp. 1–10, eds Lane, S.J. & Gilbert, J.S., Geological Society, Special Publications, 307.

Groom, D.E., Mokhov, N.V. & Striganov, S.I., 2001. Muon stopping power and range tables 10 MeV–100 TeV, *At. Data Nucl. Data Tables,* **78**(2), 183–356.

Heck, D., Knapp, J., Capdevielle, J.N., Schatz, G. & Thouw, T., 1998. *CORSIKA: A Monte Carlo code to simulate extensive air showers*. Karlsruhe University, Forschungszentrum Karlsruhe, Report FZKA 6019.

Kudryavtsev, V.A., 2009. Muon simulation codes MUSIC and MUSUN for underground physics, *Compt. Phys. Commun.,* **180,** 339–346.

Lesparre, N., Gibert, D., Marteau, J., Déclais, Y., Carbone, D. & Galichet, E., 2010. Geophysical muon imaging: feasibility and limits, *Geophys. J. Int.,* **183,** 1348–1361.

Lesparre, N., Gibert, D., Marteau, J., Komorowski, J.C., Nicollin, F. & Coutant, O., 2012. Density muon radiography of La Soufrière of GuadeloupeVolcano: comparison with geological, electrical resistivity and gravity data, *Geophys. J. Int.,* **185,** 1–14.

Lokmer, I., Bean, C.J., Saccorotti, G. & Patane, D., 2007. Moment-tensor inversion of LP events recorded on Etna in 2004 using constraints obtained from wave simulation tests, *Geophys. Res. Lett.,* **34,** L22316, doi:10.1029/2007GL031902.

Marteau, J., 2010. The OPERA global readout and GPS distribution system, *Nucl. Instrum. Meth. A,* **617,** doi:10.1016/j.nima.2009.10.095.

Marteau, J., Gibert, D., Lesparre, N., Nicollin, F., Noli, P. & Giacoppo, F., 2012. Muons tomography applied to geosciences and volcanology, *Nucl. Instrum. Meth. A,* **617,** 291–293.

Nagamine, K., 2003. *Introductory Muon Science,* Cambridge University Press, 208 pp.

Nagamine, K., Iwasaki, M., Shimomura, K. & Ishida, K., 1995. Method of probing inner-structure of geophysical substance with the horizontal cosmic-ray muons and possible application to volcanic eruption prediction, *Nucl. Instrum. Meth. A,* **356,** 585–595.

Neddermeyer, S.H. & Anderson, C.D., 1937. Note on the nature of cosmic ray particles, *Phys. Rev.,* **51,** 884–886.

Neri, M. & Acocella, V., 2006. The 2004–2005 Etna eruption: implications for flank deformation and structural behaviour of the volcano, *J. Volc. Geotherm. Res.,* **158,** 195–206.

Nettleton, L.L., 1939. Determination of density for reduction of gravimeter observations, *Geophysics,* **4,** 176–183.

Patanè, D. *et al.*, 2013. Insights into magma and fluid transfer at Mount Etna by a multiparametric approach: a model of the events leading to the 2011 eruptive cycle, *J. geophys. Res. Solid Earth,* **118,** doi:10.1002/jgrb.50248.

Pessel, M & Gibert, D, 2003. Multiscale electrical impedance tomography, *J. geophys. Res.,* **108**(B1), 2054, doi:10.1029/2001JB000233.

Reyna, D., 2006. A simple parameterization of the cosmic-ray muon momentum spectra at the surface as a function of zenith angle, preprint, arXiv:hep-ph/0604145.

Rymer, H., 1989. A contribution to precision microgravity data analysis using LaCoste and Romberg gravity meters, *Geophys. J.,* **97,** 311–322.

Saccorotti, G., Lokmer, I., Bean, C.J., Di Grazia, G. & Patane, D., 2007. Analysis of sustained long-period activity at Etna Volcano, Italy, *J. Volc. Geotherm. Res.,* **160**(3–4), 340–354.

Saracino, G. & Cârloganu, C., 2012. Looking at volcanoes with cosmic-ray muons, *Phys. Today,* **65** (12), 60–61.

Schiavone, D. & Loddo, M., 2007. 3-D density model of Mt. Etna Volcano (Southern Italy), *J. Volc. Geotherm. Res.,* **164,** 161–175.

Sciotto, M., Cannata, A., Di Grazia, G., Gresta, S., Privitera, E. & Spina, L., 2011. Seismoacoustic investigations of paroxysmal activity at Mt. Etna volcano: new insights into the 16 November 2006 eruption, *J. geophys. Res.,* **116,** B09301, doi:10.1029/2010JB008138.

Shinohara, H. & Tanaka, H.K.M., 2012. Conduit magma convention of a rhyolitic magma: constraints from cosmic-ray muon radiography of Iwodake, Satsuma-Iwojima volcano, Japan, *Earth planet. Sc. Lett.,* **349–350,** 87–97.

Tanaka, H.K.M. & Muraoka, H., 2013. Interpreting muon radiographic data in a fault zone: possible application to geothermal reservoir detection and monitoring, *Geosci. Instrum. Method. Data Syst.,* **2,** 145–150.

Downloaded from https://academic.oup.com/gji/article/196/2/633/571839 by guest on 24 April 2024

Tanaka, H.K.M. *et al.*, 2007. High resolution imaging in the inhomogeneous crust with cosmic ray muon radiography: the density structure below the volcanic crater floor of Mt. Asama, Japan, *Earth planet. Sci. Lett.,* **263,** 104–113.

Tanaka, H.K.M., Uchida, T., Tanaka, M., Shinohara, H. & Taira, H., 2009. Cosmic-ray muon imaging of magma in a conduit: degassing process of Satsuma-Iwojima Volcano, Japan, *Geophys. Res. Lett.,* **36,** L01304, doi:10.1029/2008GL036451.

Tanimoto, T., 1999. Excitation of normal modes by atmospheric turbulence: source of long-period seismic noise, *Geophys. J. Int.,* **136,** 395–402.

Tiede, C., Camacho, A.G., Gerstenecker, C., Fernández, J. & Suyanto, I., 2005. Modeling the density at Merapi volcano area, Indonesia, via the inverse gravimetric problem, *Geochem. Geophys. Geosyst.,* **6,** Q09011, doi:10.1029/2005GC000986.

Zhdanov, M.S., 2009. *Geophysical Electromagnetic Theory and Methods,* 848 pp., Elsevier.

Downloaded from https://academic.oup.com/gji/article/196/2/633/571839 by guest on 24 April 2024